Article:

Baù, D. orcid.org/0000-0002-0730-5478 (2022) Land subsidence surrogate models for normally consolidated sedimentary basins. Geomechanics for Energy and the Environment, 32. 100297. ISSN 2352-3808

https://doi.org/10.1016/j.gete.2021.100297

Land Subsidence Surrogate Models for Normally Consolidated Sedimentary Basins

Domenico Baù*

The University of Sheffield
Department Civil and Structural Engineering
Sir Frederick Mappin Building, Mappin Street, Sheffield S1 3JD, United Kingdom

Abstract

This article presents a methodology for building a computationally-fast "surrogate model" to simulate land subsidence due to fluid extraction from normally consolidated sedimentary basins. The model relies on the extension of the classic nucleus of strain solution (NoS) in a homogeneous semi-infinite continuum to heterogeneous basins, in which the uniaxial vertical compressibility c_M varies along the depth z following either a power or an exponential law. The NoS solution represents the horizontal and vertical components of the surface displacement associated with a unit volume at a given depth c in which a unit change of pore pressure occurs. The modified NoS solution is obtained by fitting the horizontal and vertical components of the surface displacement calculated using a finite-element (FE) numerical model. This is achieved through a regression algorithm that identifies four fitting parameters. By repeating such a regression over a set of combinations of the coefficients of the basin compressibility model $c_M(z)$, it is possible to identify four functions that emulate the variability of the four fitting parameters with respect to the compressibility model coefficients. The surrogate land subsidence model is then built by integrating the modified NoS equations within the subsurface region (e.g. an aquifer) where a change in pore pressure occurs due to fluid abstraction. Such formulation results in an explicit "response-matrix" approach, where the forcing terms depend on the pore pressure variations, and the matrix coefficients account for the selected basin compressibility model. The implementation approach is quite straightforward

*Corresponding author: d.bau@sheffield.ac.uk

and powerful, as it allows, for example, to easily construct a land subsidence package "online" over any groundwater flow model, or estimate "offline" the land surface displacement associated with any simulated or observed 3D pore pressure change field. The surrogate land subsidence model is tested with a series of numerical experiments, and is shown to produce accurate results within the working assumptions of the model.

Keywords: Land Subsidence, Nucleus of Strain, Model Surrogates

1. Introduction

Land subsidence is one of the major unintended effects of the extraction of fluids (water, gas, oil) from the subsurface and has long been observed worldwide, in several regions of North America (Ortiz-Zamora and Ortega-Guerrero, 2010; Castellazzi et al., 2016; Kasmarek et al., 2016; Sneed et al., 2018) and South America (de Luna et al., 2017), Europe (Teatini et al., 2006, 2012; González et al., 2012; Fokker et al., 2018), Africa (Cian et al., 2019; Ikuemonisan and Ozebo, 2020), Asia (Erban et al., 2014; Abidin et al., 2015; Wang et al., 2019), Australia and Oceania (Ng et al., 2015; Allis et al., 2009).

Land subsidence can have negative impacts on environment, economy and society, including, among others, damage to buildings and infrastructure (roads, railways, bridges, power plants, water distribution systems, wastewater treatment plants, wells, landfills, etc.), changes in flow in channel networks and drainage systems, increased flood frequency and increased sea water intrusion. As such, land subsidence has been a matter of concern in densely populated coastal regions where the elevation of the ground surface is just a few tens of centimetres above the mean sea level, where it may significantly limit the sustainability of anthropogenic activities related to subsurface development.

In recent years, the role played by land subsidence on the vulnerability of coastal regions has been even more important, as it has the potential to significantly add to the current projections of sea level rise (Kulp and Strauss, 2019). Characterizing land subsidence is thus key for urban planning and development, environmental management, as well as hydrogeological risk assessment and mitigation. Such a characterization requires the development and implementation of systematic and regular monitoring and modelling programs.

According to Galloway and Burbey (2011) mitigation of land subsidence due to groundwater withdrawal can be achieved by limiting pumping, through conjunctive use and regulating water demand, and possibly by artificial groundwater recharge. Models are key tools for predicting land displacement associated with changes in water management policies. There are essentially two categories of models that may be used for simulating the surface displacement induced by subsurface fluid extraction: numerical models and analytical models.

Numerical models rely on the solution of the classical equations of poroelasticity (Biot, 1941, 1955; Verruijt, 1969) by methods such as finite elements, finite differences, finite volumes or combinations of these. These models are quite flexible, in that they allow for simulating complex hydrogeological settings under generic conditions of heterogeneity. In some cases, they have been extended to including non-linear elastic, elasto-plastic and viscous constitutive laws and led to an unprecedented level of sophistication and accuracy in the simulation. Detailed reviews of numerical models may be found in the works of Galloway and Burbey (2011) and Gambolati and Teatini (2015).

Before numerical models, analytical models were the only tools available for simulating or predicting land subsidence due to subsurface fluid extraction. Early analytical solutions were developed by Verruijt (1969) and Bear and Corapcioglu (1981a,b), who addressed the problem of land subsidence displacement induced from the continuous pumping from a single well in an either perfectly confined or leaky aquifer. In these instances, the solution was derived through the integration of the poro-elasticity equations (Biot, 1941) using Hankel and Laplace transforms in conditions of radial symmetry and uniaxial vertical strain.

Another famous land subsidence model was presented by Geertsma (1966, 1973)), who derived a close-from analytical solution for the surface displacement induced by a disk-shaped axial-symmetric reservoir subject to a constant change in pore pressure, and embeeded in a homogeneous, linearly-elastic, semi-infinite domain. Geerstma derived his solution by integrating the so-called "nucleus of strain" (NoS) equations (Mindlin, 1936; Mindlin and Chen, 1950) over the reservoir volume. NoS equations represent the surface displacements induced by a unit change in fluid pressure, within a point source having a unit volume, and located at the same depth as the reservoir.

Following the same approach as Geertsma's, van Opstal (1974) proposed a model to estimate surface vertical displacement assuming that the reservoir lies above a rigid basement. More recently, van Opstal's models was extended by Tempone et al. (2010) to include both vertical and horizontal displacement for the full half space based on the the work of Sharma (1956).

Of related interest is also the work of Morita et al. (1989), who conducted numerical tests to derive coefficients that can be used to extend Geertsma (1973)'s solution for the land subsidence and the strain at the reservoir center, as well as the average reservoir volumetric compressibility, to those cases where a contrast between the elastic properties of the reservoir and the surrounding medium exists.

The volume integral with which Geertsma's model was obtained, relies on the hypotheses of linear elasticity and a semi-infinite system subject to homogeneous boundary conditions (i.e. no displacement) at large radial distance and depth. Such integral is practically an application of the principle of superposition of effects, in which the NoS equations (Mindlin and Chen, 1950) constitute "Green" functions. Note that it is possible to apply the same principle to reservoirs of generic shape and subject to a spatially distributed change in pore pressure. In general, such an integral would be calculated numerically, but in some particular conditions an analytical solution is possible. For example, Jayeoba et al. (2019) have recently proposed an analytical solution for the transient vertical displacement above a well pumping at a constant rate from a cylindrical confined homogeneous aquifer. Since in this instance the pore pressure change is radial-symmetric, the integration is made possible using Geertsma's vertical surface displacement at the center of a disk-shaped reservoir as the Green function.

The analytical and semi-analytical models described above heavily rely on the assumption that the reservoir and the surrounding formations are homogeneous. However, the use of NoS equations as Green functions is actually not limited by the assumption of homogeneity made by Mindlin and Chen (1950). Indeed, it is possible to extend such an approach to heterogeneous systems that do not violate the conditions radial symmetry, that is, semi-infinite domains with elastic properties varying along the depth only, as in the case, for example, of normally consolidated sedimentary basin where c_M is observed to decrease with the depth. This approach was applied by Gambolati et al. (1991) to estimate the land subsidence due to the development of a gas pool in Ravenna, Italy. In that case, however, a FE axial-symmetric model was necessary to calculate the NoS solution due to the system heterogeneity.

Nowadays numerical models constitute undoubtedly the most powerful tool for simulating land subsidence in real-world scenarios, but require conspicuous datasets to validate model assumption and calibrate. Lack of data, however, often poses significant limitations for the construction of reliable land subsidence models. In addition, these models typically imply a considerable cost in terms of time and skills for model construction and computational running time. When these limitations are tangible, analytically based closed-form solutions have the advantage of being less data-demanding, easier and faster to implement, as well as computationally more efficient.

The advantages of closed-form solutions become even more relevant when the sparsity and the uncertainty in geomechanical data need to be addressed through uncertainty quantification analyses for purposes, for example, of quantitative risk assessment in support of decision making. These analyses are typically based on Monte Carlo stochastic simulations, which may require on the order of hundreds or thousands of model runs, which may result quite overwhelming when using fully numerical models. While in these situations analytical or semi-analytical models appear to be better suited than numerical models, it is also important to improve their ability to deal with more realistic conditions of heterogeneity, such as those observed in normally consolidated sedimentary basins.

This article presents a novel, computationally-fast surrogate land subsidence models that relies on the extension of the NoS equations for normally consolidated sedimentary basins, where the uniaxial vertical compressibility c_M decreases with the depth according to either a power or an exponential model. Such a model is developed around three major components: a basin compressibility model, a semi-analytical surrogate form of the NoS equations for heterogeneous subsurface systems, and finally a surrogate land subsidence model. These components are presented in Sections 2, 3, and 4, respectively.

2. Compressibility Models in Normally Consolidated Sedimentary Basins

Considered here is the case of a fully saturated sedimentary basin in condition of "normal consolidation", that is, where the compaction in any given point depends solely on the current effective stress exerted by the "overburden", and no overloading has ever occurred. In such a basin, the total vertical stress σ_z at any given depth z can be estimated as:

$$\sigma_z(z) = \int_0^z \rho_{bw}(z') \cdot g \cdot dz' \tag{1}$$

where g is gravity, and ρ_{bw} is the wet bulk density, given by:

$$\rho_{bw} = \rho_s \cdot (1 - \phi) + \rho_w \cdot \phi \tag{2}$$

In Eq. (2), ρ_s is the solid density, ρ_w is the water density, and ϕ is the porosity. While all these properties may vary with z, ρ_s and ρ_w are assumed to be constant (ρ_s=2650 kg/m^3; ρ_w=1000 kg/m^3). The so-called "overburden gradient" $obg(z)$ is associated with $\sigma_z(z)$ by the following relationship:

$$obg(z) = \frac{\sigma_z(z)}{z} \tag{3}$$

Because of Eq. (1), $obg(z)$ represents the average soil specific weight ($\rho_{bw} \cdot g$) over the "column" $[0, z]$. Assuming the pore pressure p as hydrostatically distributed (i.e. $p = \rho_w \cdot g \cdot z$), Terzaghi's principle establishes a link between the total vertical stress σ_z and the effective vertical stress σ'_z at any depth z (Terzaghi, 1936):

$$\sigma_z(z) = \alpha \cdot \rho_w \cdot g \cdot z + \sigma'_z(z) \tag{4}$$

where α is Biot's coefficient (Biot, 1941; Biot and Willis, 1957), expressed as:

$$\alpha = 1 - \frac{c_s}{c_M} \tag{5}$$

with c_s being the compressibility of the particles (solid phase). Merging Eqs. (3) and (4) yields the following relation between the overburden gradient and the vertical effective stress:

$$\sigma'_z(z) = obg(z) \cdot z - \alpha \cdot \rho_w \cdot g \cdot z \tag{6}$$

It is worth pointing out that, within the normal consolidation assumption, the sedimentary basin is assumed to have been formed under a ”slow” and “homogeneous” deposition process. In this process, the progressive increase in total stress produces a consolidation of the porous medium, in which the in-situ porosity decreases as z and thus σ'_z increase (Eq. 6). It is then possible to derive an expression for the basin compressibility c_M as a function of z based on the variations of ϕ observed through the overburden gradient $obg(z)$. To do so, two assumptions are made: (a) soil particles are incompressible; and (b) the porous medium undergoes no horizontal strain (oedometric conditions).

Note that hypothesis (a) applies to “soft” porous media, in which c_s is negligible with respect to c_M, so that $\alpha \cong 1$ (Eq. 5). This is typically justifiable since c_s is of the order of 10^{-11}-10^{-10} Pa^{-1} for most common sediment minerals (Zisman, 1933).

For a representative elementary porous volume (REV) of thickness H subject, during deposition, to a thickness reduction dH due to an effective stress increase $d\sigma'_z$, the uniaxial vertical compressibility is defined as:

$$c_M = -\frac{1}{H} \cdot \frac{dH}{d\sigma'_z} \tag{7}$$

Since the sample volume V and the solid phase volume V_s are related to one another by $V_s = V \cdot (1 - \phi)$, and taking into account of the grain incompressibility and the oedometric assumptions, the following is relation is obtained:

$$dV_s = d\left[V \cdot (1 - \phi)\right] = A \cdot d\left[H \cdot (1 - \phi)\right] = 0 \tag{8}$$

where A is the REV base area $(V = A \cdot H)$. From Eq. (8):

$$dH \cdot (1 - \phi) - H \cdot d\phi = 0 \tag{9}$$

and thus:

$$\frac{dH}{H} = \frac{d\phi}{1 - \phi} \tag{10}$$

Substituting Eq. (10) in (7) yields:

$$c_M = -\frac{1}{1 - \phi} \cdot \frac{d\phi}{d\sigma'_z} \tag{11}$$

Eq. (11) provides a basis for exploring the relationships between c_M, σ'_z and z. By taking the derivative with respect to z of Eq. (1), and using Eqs. (2) and (3):

$$\frac{d}{dz}\left[obg\left(z\right) \cdot z\right] = \frac{d}{dz}\int_0^z \left\{\rho_s \cdot \left[1 - \phi\left(z'\right)\right] + \rho_w \cdot \phi\left(z'\right)\right\} \cdot g \cdot dz' = \rho_s \cdot g - (\rho_s - \rho_w) \cdot g \cdot \phi\left(z\right) \tag{12}$$

Eq. (12) can be rearranged to obtain ϕ as a function of $obg\left(z\right)$ and z:

$$\phi\left(z\right) = \frac{\rho_s}{\rho_s - \rho_w} - \frac{1}{(\rho_s - \rho_w) \cdot g} \cdot \frac{d}{dz}\left[obg\left(z\right) \cdot z\right] \tag{13}$$

Eq. (13) is the first element needed to evaluate Eq. (11). $\frac{d\phi}{d\sigma'_z}$ can be calculated by noting that: $\frac{d\phi}{d\sigma'_z} = \frac{d\phi}{dz} / \frac{d\sigma'_z}{dz}$. From Eq. (13):

$$\frac{d\phi}{dz} = -\frac{\frac{d^2}{dz^2}\left[obg\left(z\right) \cdot z\right]}{(\rho_s - \rho_w) \cdot g} \tag{14}$$

and from Eq. (6):

$$\frac{d\sigma'_z}{dz} = \frac{d}{dz}\left[obg\left(z\right) \cdot z\right] - \rho_w \cdot g \tag{15}$$

Substituting Eqs. (13-15) into (11) gives, after a few rearrangements:

$$c_M\left(z\right) = \frac{\frac{d^2}{dz^2}\left[obg\left(z\right) \cdot z\right]}{\left\{\frac{d}{dz}\left[obg\left(z\right) \cdot z\right] - \rho_w \cdot g\right\}^2} \tag{16}$$

Eq. (16) can be used to estimate $c_M(z)$ from $obg(z)$. One can observe that if $obg(z) \cdot z$, that is $\sigma_z(z)$, is linear, then $c_M(z) = 0$, that is, the porous medium results incompressible. Thus, in a normally consolidated basin, for $c_M(z)$ to be positive, $\sigma_z(z)$ must be a convex function.

The derivation of Eq. (16) is valid so long as $\alpha = 1$, which, for practical applications, requires c_M to be at least 10 times larger than c_s. This translates into a maximum depth value, within which c_M is correctly estimated by Eq. (16). Such a value depends on the adopted overburden gradient model $obg(z)$. Beyond that depth one can assume that, since the porosity cannot be further reduced, the compressibility of the continuum approaches c_s.

Note that the combination of Eqs. (6) and (16) would allow for deriving an implicit non-linear elastic constitutive law, which could be used to simulate changes of c_M occurring due to fluid abstraction. This approach was followed, for example, by Baú et al. (2002) and Ferronato et al. (2003), but is not used here. Instead, a plain linear-elastic model is adopted, which assumes that during depletion c_M remains constant and equal to the in-situ conditions prior to fluid abstraction (Eq. 16).

2.1. Homogeneous Systems

In a basin characterized by a homogeneous c_M, Eq. (11) can be easily integrated by separation of variables to derive the following porosity function:

$$\phi(z) = 1 - (1 - \phi_0) \cdot e^{c_M \cdot \sigma'_z(z)} \tag{17}$$

where the boundary conditions $\phi(0) = \phi_0$ and $\sigma'(0) = 0$ have been imposed. From Eqs. (1-2) and (4):

$$\sigma'_z(z) = \int_0^z (\rho_s - \rho_w) \cdot (1 - \phi) \cdot g \cdot dz' \tag{18}$$

Substituting Eq. (17) into (18) yields:

$$\sigma'_z(z) = (\rho_s - \rho_w) \cdot g \cdot (1 - \phi_0) \cdot \int_0^z e^{c_M \cdot \sigma'_z(z')} \cdot dz' \tag{19}$$

The integral function at the right-hand side of Eq. (19) is removed by taking the derivative of it with respect to z, which produces:

$$\frac{d\sigma'_z(z)}{dz} = (\rho_s - \rho_w) \cdot g \cdot (1 - \phi_0) \cdot e^{c_M \cdot \sigma'_z(z)} \tag{20}$$

Eq. (20) can be integrated by separation of variables, which leads to the following expression:

$$\sigma'_z(z) = -\frac{1}{c_M} \cdot \ln\left[1 - c_M \cdot (\rho_s - \rho_w) \cdot g \cdot (1 - \phi_0) \cdot z\right] \tag{21}$$

Substituting Eq. (21) into (17) allows to determine the porosity:

$$\phi(z) = 1 - \frac{1 - \phi_0}{1 - c_M \cdot (\rho_s - \rho_w) \cdot g \cdot (1 - \phi_0) \cdot z} \tag{22}$$

Substituting Eq. (21) into (4) provides the total stress:

$$\sigma_z(z) = \rho_w \cdot g \cdot z - \frac{1}{c_M} \cdot \ln\left[1 - c_M \cdot (\rho_s - \rho_w) \cdot g \cdot (1 - \phi_0) \cdot z\right] \tag{23}$$

The overburden gradient (Eq. 3) can thus be expressed as:

$$obg(z) = \rho_w \cdot g - \frac{\ln\left[1 - c_M \cdot (\rho_s - \rho_w) \cdot g \cdot (1 - \phi_0) \cdot z\right]}{c_M \cdot z} \tag{24}$$

Example profiles for $\phi(z)$ (Eq. 22) and $obg(z)$ (Eq. 24) are given in Figure 1 (see the blue solid lines).

Note that Eq. (22) holds so long as $\phi(z) \geq 0$. According to such a model, the porosity decreases with the depth, from ϕ_0 at $z = 0$, to zero at a depth $z = z_{max}$, so that Eq. (22) can be deemed valid only if:

$$0 \leq z \leq z_{max} = \frac{\phi_0}{1 - \phi_0} \cdot \frac{1}{c_M \cdot (\rho_s - \rho_w) \cdot g} \tag{25}$$

The constraints (25) reveal that the conditions of normal consolidation and homogenous c_M result incompatible beyond the depth z_{max}. Indeed, since at that depth the porosity vanishes, the porous medium underneath behaves like an elastic continuum, with a compressibility c_s that is much smaller than c_M, which violates the homogeneity assumption.

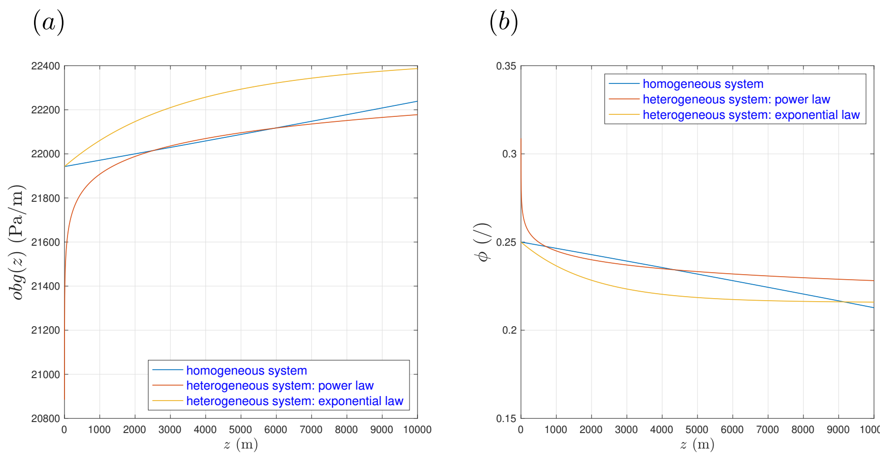

Figure 1: Examples of (a) overburden gradient and (b) porosity profiles vs. depth for normally consolidated sedimentary basins where c_M is considered either homogeneous, or heterogeneous according to a power law (Eq. 30) and an exponential law (Eq. 36).

2.2. The Heterogeneous Case

Let us now consider a hypothetical basin where the vertical effective stress increases with depth according to a power law:

$$\sigma_z'(z) = a_1 \cdot z^{b_1} \tag{26}$$

where a_1 and b_1 are two strictly positive coefficients. Based on Eq. (4), the total vertical stress is:

$$\sigma_z(z) = \rho_w \cdot g \cdot z + a_1 \cdot z^{b_1} \tag{27}$$

and the overburden gradient (Eq. (3)) is:

$$obg(z) = \rho_w \cdot g + a_1 \cdot z^{b_1 - 1} \tag{28}$$

The power law (26) is thus adequate for sedimentary basins in which overburden data, typically calculated from density logs (Ellis and Singer, 2008), can be fit to a function such as (28). Substituting Eq. (28) into (13) yields:

$$\phi(z) = 1 - \frac{a_1 \cdot b_1 \cdot z^{b_1 - 1}}{(\rho_s - \rho_w) \cdot g} \tag{29}$$

Figure 1 shows example profiles (the orange solid lines) for $obg\left(z\right)$ and $\phi\left(z\right)$ based on Eqs. (28) and (29).

Substituting Eq. (28) into (16) gives the basin compressibility:

$$c_M\left(z\right) = \frac{b_1 - 1}{a_1 \cdot b_1} \cdot z^{-b_1} \tag{30}$$

Basin compressibilty models based on Eq. (30) have been derived and adopted for land subsidence simulation by, among others, Baú et al. (2002), Ferronato et al. (2003), Teatini et al. (2011), and Jha et al. (2015).

Note that for c_M to be strictly positive, the condition $b_1 > 1$ must hold. In turn, since ϕ (Eq. 29) needs be theoretically between 0 and 1, the following condition is also necessary:

$$0 < \frac{a_1 \cdot b_1 \cdot z^{b_1 - 1}}{\left(\rho_s - \rho_w\right) \cdot g} \leq 1 \tag{31}$$

Such inequality is met if:

$$0 \leq z \leq z_{max} = \left[\frac{\left(\rho_s - \rho_w\right) \cdot g}{a_1 \cdot b_1}\right]^{\frac{1}{b_1 - 1}} \tag{32}$$

Similar to (25), condition (32) indicates that at depth larger than z_{max} the porosity vanishes, and the porous medium behaves like an elastic continuum, with a negligible compressibility or, in other words, an almost rigid basement. One may also observe that, according to Eq. (29), the porosity at $z = 0$ is equal to 1, which implies unrealistically high values of ϕ at shallow depth. This may be observed from the orange profiles in Figure 1b.

An attractive alternative to the power compressibility model (Eqs. 26-30) may be derived by assuming an “exponential” porosity model:

$$\phi\left(z\right) = \phi_{min} + \left(\phi_0 - \phi_{min}\right) \cdot e^{-\frac{z}{\lambda}} \tag{33}$$

where ϕ_0 and ϕ_{min} are the porosity values at $z = 0$ and $z \to \infty$, and λ is a scale length that regulates the rate of decrease of ϕ along the depth z. This model appears to be more robust than the previous one, since realistic values of ϕ can be prescribed even at shallow depth. In addition, the porosity vanishes asymptotically (i.e., only at large depth) and no constraints, such as (25) and (32), are needed.

Based on Eqs. (1-2), the total vertical stress associated with the porosity model (33) is given by:

$$\begin{aligned}\sigma_z(z) = {} & [\rho_s \cdot (1-\phi_{min}) + \rho_w \cdot \phi_{min}] \cdot g \cdot z \\ & + (\rho_s - \rho_w) \cdot (\phi_0 - \phi_{min}) \cdot g \cdot \lambda \cdot \left(e^{-\frac{z}{\lambda}} - 1\right)\end{aligned} \tag{34}$$

from which (Eq. (3)):

$$obg(z) = [\rho_s \cdot (1-\phi_{min}) + \rho_w \cdot \phi_{min}] \cdot g + (\rho_s - \rho_w) \cdot (\phi_0 - \phi_{min}) \cdot g \cdot \lambda \cdot \frac{e^{-\frac{z}{\lambda}} - 1}{z} \tag{35}$$

Example profiles for $\phi(z)$ (Eq. (33)) and $obg(z)$ (Eq. (35)) are given by the yellow solid lines in Figure 1.

The compressibility $c_M(z)$ associated with the exponential porosity model (Eq. (33)) can be calculated by substituting Eq. (35) into (16), which yields:

$$c_M(z) = \frac{(\phi_0 - \phi_{min})}{(\rho_s - \rho_w) \cdot g \cdot \lambda} \cdot e^{-\frac{z}{\lambda}} \tag{36}$$

According to Eq. (36), c_M decreases exponentially with z, from a surficial value equal to $\frac{(\phi_0 - \phi_{min})}{(\rho_s - \rho_w) \cdot g \cdot \lambda}$, to zero asymptotically.

Here, it is worth highlighting the role played by the scaling coefficient λ. Low values of λ represent highly compressible and heterogeneous basins, where c_M decreases sharply as z increases. Vice versa, large values of λ represent generally low-compressible and pseudo-homogeneous basins, where c_M is reduced very smoothly as z increases.

3. The Nucleus of Strain Equations

The nucleus of strain (NoS) equations (Mindlin, 1936; Mindlin and Chen, 1950; Geertsma, 1966) describe the displacement of the traction-free horizontal surface of a three-dimensional homogeneous semi-infinite system, in which a unit increase in pore pressure occurs in a small unit volume located at depth c from the surface (Figure 2). The horizontal and vertical displacement components

(u_h, u_v) are (Geertsma, 1973):

$$\begin{aligned} &\text{(a):} \quad u_h(r) = \frac{c_M^* \cdot (1-\nu)}{\pi} \cdot \frac{r}{\left(c^2+r^2\right)^{1.5}} \\ &\text{(b):} \quad u_v(r) = \frac{c_M^* \cdot (1-\nu)}{\pi} \cdot \frac{c}{\left(c^2+r^2\right)^{1.5}} \end{aligned} \tag{37}$$

where c_M^* and ν are the vertical uniaxial compressibility and the Poisson ratio of the (homogeneous) porous medium, respectively, and r is the radial coordinate with respect to a vertical axis crossing the NoS location. Note that since $u_h/u_v = r/c$, u_h and u_v are equal for $r = c$.

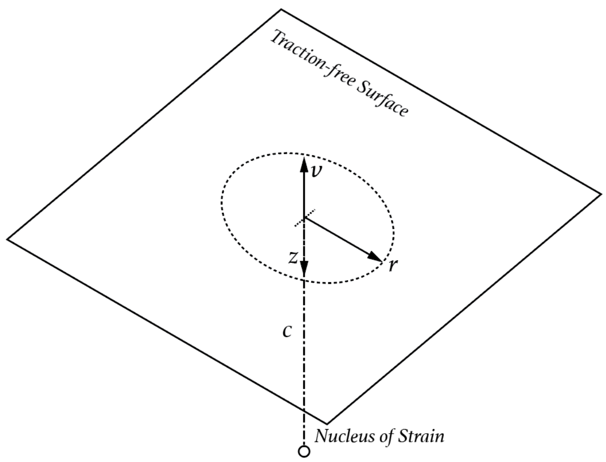

Figure 2: Three-dimensional semi-infinite space in which the NoS is situated. Because of the homogeneity assumption, the displacement components are symmetric with respect the vertical axis crossing the NoS.

For this analysis, it comes in handy to normalize Eqs. (37) with respect to the displacement $u_v(0) = \frac{c_M^* \cdot (1-\nu)}{\pi \cdot c^2}$, which leads the following dimensionless NoS equations:

$$\begin{aligned} &\text{(a):} \quad \overline{u_h}(r) = \frac{u_h(r)}{\frac{c_M^* \cdot (1-\nu)}{\pi \cdot c^2}} = \frac{c^2 \cdot r}{\left(c^2+r^2\right)^{1.5}} \\ &\text{(b):} \quad \overline{u_v}(r) = \frac{u_v(r)}{\frac{c_M^* \cdot (1-\nu)}{\pi \cdot c^2}} = \frac{c^3}{\left(c^2+r^2\right)^{1.5}} \end{aligned} \tag{38}$$

Introducing the dimensionless radial coordinate $R = r/c$ in Eqs. (38) yields:

$$\begin{aligned} &\text{(a):} \quad \overline{u_h}\,(R) = R \cdot \left(1 + R^2\right)^{-1.5} \\ &\text{(b):} \quad \overline{u_v}\,(R) = \left(1 + R^2\right)^{-1.5} \end{aligned} \tag{39}$$

Eqs. (39) indicate that the normalized NoS displacement components depend on the scaled radial coordinate R, rather than the radial coordinate r itself. Note also that since the NoS depth c is not an independent variable for $\overline{u_h}\,(R)$ and $\overline{u_v}\,(R)$, these are invariant with respect to c. This is due to the nature of the system, which is semi-infinite, and any variation of c is equivalent to a simple change of the spatial scale. Consequently the shape of the displacement bowl remains the same, while only the displacement amplitude is changed.

The NoS Eqs. (37) may be used to assess the land subsidence due to fluid extraction from subsurface formations (see Section 4), using a value of c_M estimated at the formation depth (Geertsma, 1966, 1973). For example, in the case of the compressibility model (30) the medium compressibility c_M^* is:

$$c_{M,1}^* = \frac{b_1 - 1}{a_1 \cdot b_1} \cdot c^{-b_1} \tag{40}$$

Eq. (40) allows for expressing Eq. (30) in the following equivalent form:

$$c_M\,(z) = c_{M,1}^* \cdot \left(\frac{z}{c}\right)^{-b_1} \tag{41}$$

Similarly, in the case of the compressibility model (36) the medium compressibility c_M^* takes on the value:

$$c_{M,2}^* = \frac{(\phi_0 - \phi_{min})}{(\rho_s - \rho_w) \cdot g \cdot \lambda} \cdot e^{-\frac{c}{\lambda}} \tag{42}$$

Using Eq. (40), Eq. (36) can be modified as:

$$c_M\,(z) = c_{M,2}^* \cdot e^{-\frac{z-c}{\lambda}} \tag{43}$$

Figure 3 shows the profiles of c_M vs. z according to Eqs. (41) (the orange solid line) and (43) (the yellow solid line). In these examples, the two profiles are characterized by the same compressibility value c_M^* at a NoS depth c = 2,000 m. The same value is used to draw the profile of $c_M(z)$ in the homogeneous case (the blue solid line).

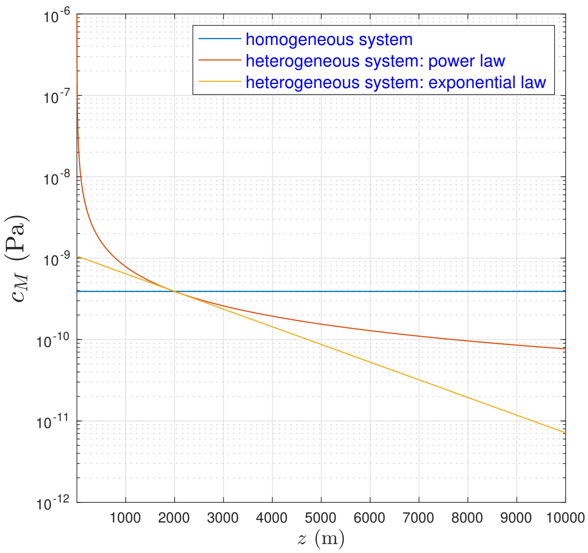

Figure 3: Examples of compressibility models for normally consolidated sedimentary basins where c_M is either constant, or decreasing with the depth according to a power law (Eq. (30)) or an exponential law (Eq. 36)).

Eqs. (41) and (43) show that $c_M(z) \geq c_M^*$ for $0 \leq z \leq c$, and $c_M(z) < c_M^*$ for $z > c$ (see also Figure 3). In both scenarios, the porous medium is stiffer below and softer above the depth c with respect to the homogeneous case. Consequently, the homogeneity assumption is likely to lead to an underestimation of the surface displacement. The amplitude of this error depends largely on the degree of heterogeneity of c_M, which is determined by the coefficients b_1 and λ for the compressibility models (41) and (43), respectively.

It is worth noting that the NoS Eqs. (37) and (39) are valid under the homogeneity assumption, which, however idealized, is subject to the constraint (25). In practical terms, it seems reasonable to apply Eqs. (37) if the depth z_{max} in Equation (25) is significantly larger, say 10 times, than c, since at this depth the displacement amplitude is negligible compared to that at the surface. And since z_{max} is inversely proportional to c_M (see Eq. (25)), such application seems more suited for low-compressible basins. By imposing the condition $z_{max} \geq 10 \cdot c$, the following constraint is thus derived:

$$c_M \leq c^*_{M,max} = \frac{\phi_0}{1-\phi_0} \cdot \frac{1}{\cdot(\rho_s - \rho_w) \cdot g \cdot 10 \cdot c} \tag{44}$$

where $c^*_{M,max}$ represents the compressibility upper bound that ensures that the hypothesis of homogeneity is physically meaningful for the application of the NoS equations (37). Inequality (44) indicates that $c^*_{M,max}$ is inversely proportional the NoS depth c, and increases with the surface porosity ϕ_0. Profiles of $c^*_{M,max}$ vs. ϕ_0 are graphed in Figure 4 for different values of c. "Feasible" values of c_M are represented by the regions below each of the profiles.

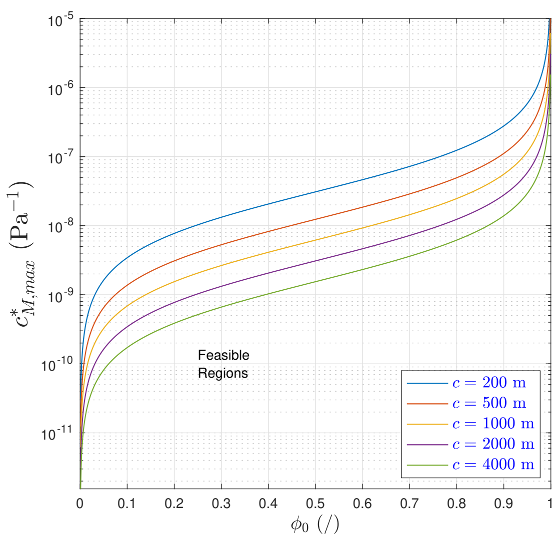

Figure 4: Feasible regions of the homogeneous compressibility c_M as functions of the surface porosity ϕ_0 and the NoS depth c. Note, for example, that for values of ϕ_0 around 0.4, and c=2000 m, c^*_M should not exceed 2×10^{-9} Pa^{-1}.

3.1. The heterogeneous case

The main goal of this work is derive surrogate forms of Eqs. (37) applicable to sedimentary basins with a compressibility heterogeneously distributed as in Eqs. (30) and (36). This analysis relies on an extensive series of numerical tests conducted using the finite-element (FE) model SUBAXS (Gambolati et al., 2001), which solves the equilibrium equations governing the deformation of an axial-symmetric medium. Such a model uses a “infinite gradient” formulation to simulate reservoirs with a pore pressure discontinuity at their boundary, and is thus particularly suited to simulate the NoS effects.

3.1.1. Numerical setup

In these numerical tests, the semi-infinite domain is approximated by a cylindrical domain with a 50,000-m radius and a 20,000-m depth, with the NoS located on the cylinder axis at depth c=2,000 m from the upper boundary. Both the lower and the lateral boundaries of the domain are subject to no-displacement constraints, while the upper boundary, representing the land surface, is “traction-free”, that is, unconstrained. Because of the radial symmetry, the three-dimensional (3D) problem is reduced to a two-dimensional (2D), axial-symmetric problem. Such setting is depicted in Figure 5.

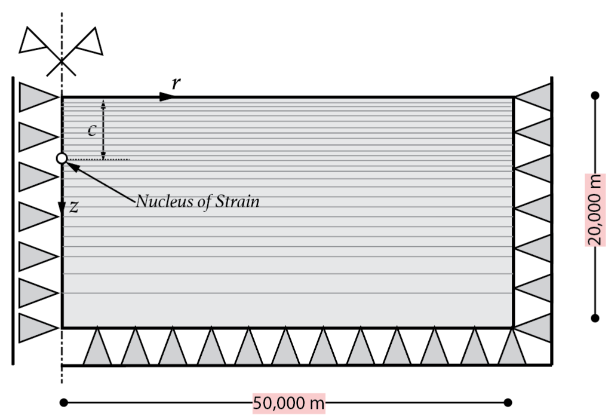

Figure 5: Axial-symmetric conceptual model for the FE simulation of the surface displacement components associated with the NoS. The surface boundary is unconstrained and the left boundary (*i.e.* the axial-symmetry axis) is fixed horizontally ($u_h = 0$). Both the bottom and the lateral boundaries are fully fixed ($u_h = u_v = 0$).

To discretize such system, a FE mesh is created with 64,186 nodes and 127,148 triangular elements. The mesh includes 291 horizontal layers characterised by different values of c_M based on the compressibility models (30) and (36). A uniformly distributed change in pore pressure of $\Delta p = 1$ Pa is prescribed within the elements of a “small” cylinder, of radius r_r=10 m and thickness b_r=10 m, centered at the location of the NoS. In order to calculate the surface displacement components associated with the NoS, the surface displacements obtained numerically are divided by $V_r \cdot \Delta p$, where $V_r = b_r \pi r_r^2$ is the volume of the ”activated” cylinder. Figure 6 shows a comparison of the surface displacement profiles obtained with the analytical solution (39) and with SUB-AXS. The differences are negligible, which indicates the constructed FE mesh has a sufficiently fine resolution.

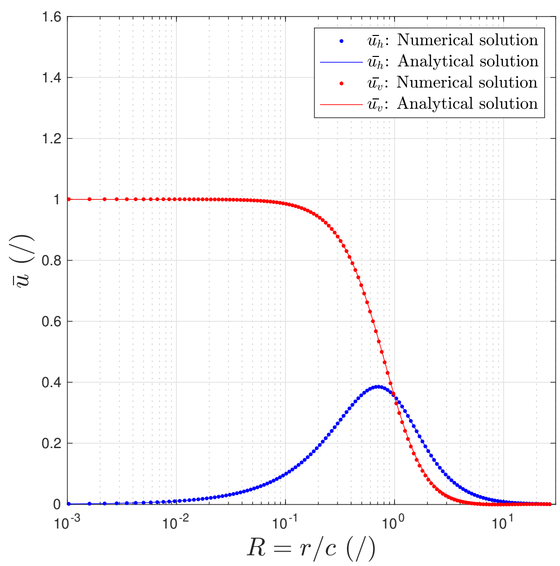

Figure 6: Radial profiles of the surface displacement horizontal and vertical components for a generic nucleus of strain located at depth c, obtained analytically (solid lines) and numerically (dotted lines). The displacements are normalised with respect to the axial vertical surface displacement (Eq. 37b for r=0), whereas the radial distance is scaled with respect to the NoS depth, c.

3.1.2. NoS Semi-analytical Solution

Preliminary numerical tests conducted with SUBAXS reveal that Eqs. (39) can be extended to the conditions of heterogeneity of sedimentary basins characterised by the compressibility models (41) and (43). The following normalized NoS equations are thus proposed:

$$\begin{aligned} &\text{(a):} \quad \overline{u_h}(R) = \alpha_h \cdot R \cdot \left(1+R^2\right)^{\beta_h} \\ &\text{(b):} \quad \overline{u_v}(R) = \alpha_v \cdot \left(1+R^2\right)^{\beta_v} \end{aligned} \tag{45}$$

where α_h, β_h, α_v, and β_v are coefficients to be determined by fitting the Eqs. (45) to the numerical solutions obtained using SUBAXS (see Section 3.1.3). Once these coefficients are calculated, the Eqs. (45) are substituted back into Eqs. (37) in place of Eqs. (39), which leads to the following surrogate NoS solution:

$$\begin{aligned} &\text{(a):} \quad u_h(r) = \frac{c_M^* \cdot (1-\nu)}{\pi \cdot c^2} \cdot \alpha_h \cdot \frac{r}{c} \cdot \left[1+\left(\frac{r}{c}\right)^2\right]^{\beta_h} \\ &\text{(b):} \quad u_v(r) = \frac{c_M^* \cdot (1-\nu)}{\pi \cdot c^2} \cdot \alpha_v \cdot \left[1+\left(\frac{r}{c}\right)^2\right]^{\beta_v} \end{aligned} \tag{46}$$

In Eqs. (46), c_M^* represents the vertical uniaxial compressibility calculated at the depth c, that is, $c_{M,1}^*$ (Eq. 40) for the compressibility power model, and $c_{M,2}^*$ (Eq. 42) for the compressibility exponential model.

Using basic principles of linear elasticity, it is possible to demonstrate that, even in the heterogeneous case, the normalized displacement functions $\overline{u_h}(R)$ and $\overline{u_v}(R)$ (Eqs. (45)) do not depend on the NoS depth c, and thus on the c_M^* value, but only of the degree of heterogeneity of c_M, as quantified by b_1 for the compressibility model (41), and by the length λ scaled to the NoS depth c, that is $\lambda' = \lambda/c$, for the compressibility model (43).

This is has important implications on the computational cost of this analysis, since the coefficients α_h, β_h, α_v and β_v can be quantified using a single reference value of c, which is set to 2,000 m in these tests. Of course, the NoS depth will still affect the actual surface displacement amplitude through the terms c and c_M^* in Eqs. (46).

3.1.3. Fitting Approach

The coefficients α_h, β_h, α_v and β_v of the surrogate NoS Eqs. (45) can be determined by minimising separately the square residual non-linear functions:

$$\begin{aligned} &\text{(a):} \quad F_h\left(\alpha_h, \beta_h\right) = \sum_{i=1}^{N_s} \left[\overline{u_h}\left(R_i\right) - \overline{u_h}_i\right]^2 \\ &\text{(b):} \quad F_v\left(\alpha_v, \beta_v\right) = \sum_{i=1}^{N_s} \left[\overline{u_v}\left(R_i\right) - \overline{u_v}_i\right]^2 \end{aligned} \tag{47}$$

where $(\overline{u_h}_i, \overline{u_v}_i)$ are the normalized NoS displacement components calculated –numerically– at the generic surface node i ($i = 1, 2, ..., N_s$) of the 2D grid used to discretize the subsurface system, and $\left(\overline{u_h}\left(R_i\right), \overline{u_v}\left(R_i\right)\right)$ are the corresponding components calculated using Eqs. (45). The minimization of the two functions $F_h\left(\alpha_h, \beta_h\right)$ and $F_v\left(\alpha_v, \beta_v\right)$ is here carried out using a non-linear least-square technique, such as the "trust-region-reflective" method (Coleman and Li, 1996).

Examples of fit results are presented in Figure 7, which shows the profiles of the displacement components $\overline{u_h}(R)$ and $\overline{u_v}(R)$, along with the fitted profiles based on Eqs. (45), with the coefficients α_h, β_h, α_v, and β_v calculated by minimizing Eqs. (47). Figure 7a reports the case of a power compressibility model (Eq. 41) with $b_1 = 1.1$, for which the resulting fitting coefficients are: $\alpha_h = 3.21097$, $\beta_h = -2.04310$, $\alpha_v = 1.51600$, and $\beta_v = -2.02741$. Likewise, Figure 7b reports the case of an exponential compressibility model (Eq. 43) with $\lambda/c = 1$, for which the resulting fitting coefficients are: $\alpha_h = 1.81680$, $\beta_h = -1.78647$, $\alpha_v = 1.47040$, and $\beta_v = -1.93010$.

For both compressibility laws, the fit of the NoS Eqs. (45) to the numerical solution is deemed satisfactory. Some minor discrepancies are observed for large R values, where the numerical displacement values result somewhat smaller than the fitted displacement profiles. These discrepancies are due to the approximation introduced in the numerical simulation by setting up the semi-infinite space as a laterally finite cylindric domain with a fixed lateral boundary, and are expected to have a negligible impact on overall displacement results, as they are limited to lower-order of magnitude displacements occurring at large radial distance.

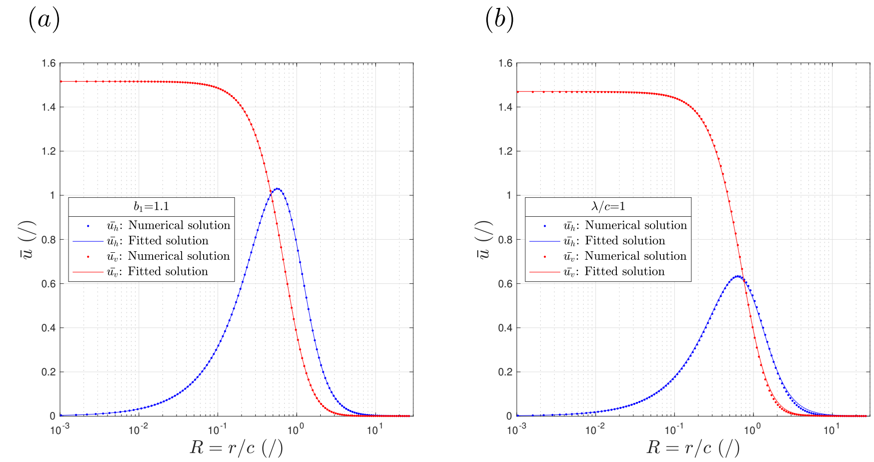

Figure 7: Fitted profiles of the normalized NoS displacement components $\overline{u_h}$ and $\overline{u_v}$ vs. the scaled radial distance $R = r/c$ obtained in the cases of: (a) a power compressibility model (Eq. (41)) with $b_1 = 1.1$; (b) an exponential compressibility model (Eq. (41)) with $\lambda/c = 1$.

3.1.4. Characterizing the Basin Compressibility Model Heterogeneity

In order to extend the NoS Eqs. (45) to the heterogeneity conditions represented by the compressibility models (41) and (43) it is necessary to derive closed-form expressions of the coefficients α_h, β_h, α_v, and β_v as functions of the parameters b_1 and λ/c. To do so, it is important to first identify the intervals of variability of b_1 and λ.

In the case of the compressibility model (41), one needs to recall the constraint (32) and derive a condition similar to inequality (44) for the homogeneous case. The following inequality is thus imposed:

$$z_{max} = \left[\frac{(\rho_s - \rho_w) \cdot g}{a_1 \cdot b_1}\right]^{\frac{1}{b_1 - 1}} \geq 10 \cdot c \tag{48}$$

The last relationship cannot be made explicit with respect to b_1. However, by extracting the term $a_1 \cdot b_1$ from Equation (40) and substituting it in (48) provides:

$$c^*_{M,1} \geq c^*_{M,1_{min}} = \frac{(b_1 - 1) \cdot 10^{b_1 - 1}}{(\rho_s - \rho_w) \cdot g \cdot c} \tag{49}$$

Inequality (49) quantifies the minimum value of the compressibility $c^*_{M,1}$ for any given value of b_1>1. These conditions are graphed in Figure 8 for several depth values. Each profile delimits the feasible region of all possible combinations of $c^*_{M,1}$ and b_1. While Figure 8 indicates b_1 has no upper bound, typical values of it are between 1 and 1.5. Indeed (see Eq. (30)), b_1 represents the reduction in order of magnitude of c_M per order of magnitude of depth increase. Such effect is graphed in Figure 9a, which shows a series of profiles of c_M vs. z for increasing values of b_1. The latter represents the negative slope of the c_M vs. z profile on a double-log plot. A value b_1=3, for example, implies that the basin compressibility decreases by as many as 1×10^3 times from a depth of 200 m, down to a depth of 2000 m, which appears to be a far-fetched scenario.

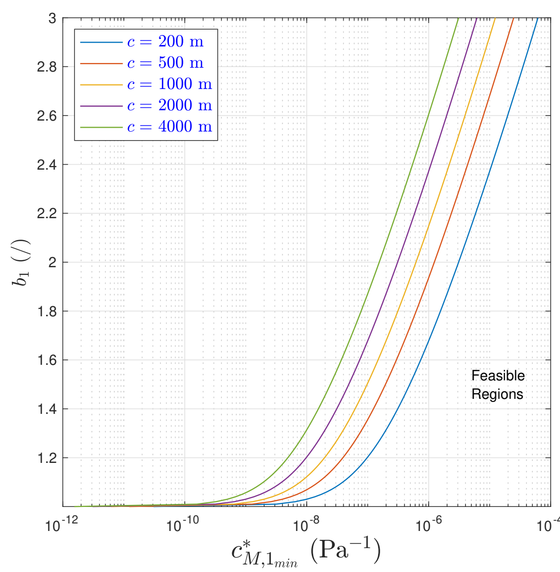

Figure 8: Feasible regions for the compressibility $c^*_{M,1}$ as function of the power coefficient b_1 for several values of the depth c (see condition (49)).

In addition, based on the profiles in Figure 8, b_1 values greater than 1.5 are viable only for relatively large values of the compressibility $c^*_{M,1}$. For example, for c=2000 m, a value of b_1=2 is possible only if $c^*_{M,1} \geq c^*_{M,1_{min}} = 3\times10^{-7}$ Pa^{-1}, which would be representative of an unusually compressible sedimentary basin.

Figure 9b shows the ϕ vs. z profiles obtained using Equation (29), for a

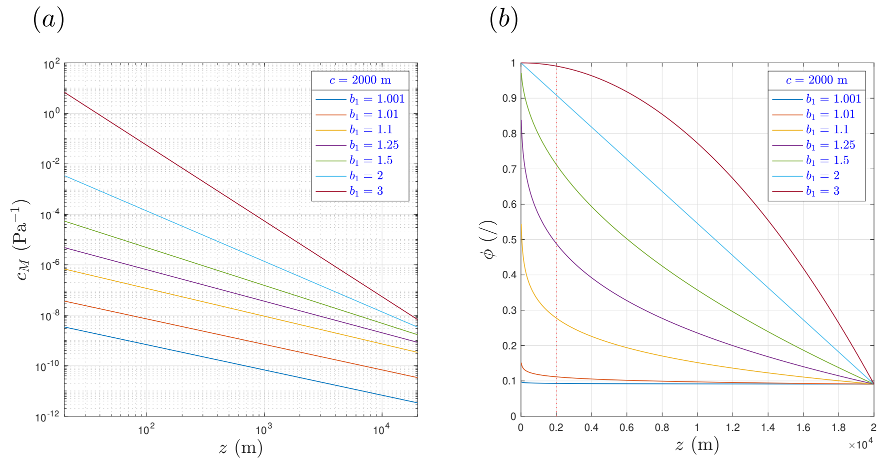

Figure 9: Profiles of (a) c_M vs. z and (b) ϕ vs. z according to a power model with increasing values of b_1, for a reference NoS depth $c = 2000$ m. In each instance, a $c^*_{M,1}$ value equal to $1.1{\cdot}c^*_{M,1,min}$ (see Eq. (49)) is selected.

reference depth $c = 2000$ m, different values of b_1, and assuming $c^*_{M,1}$ values slightly larger than $c^*_{M,1_{min}}$ (see (49)). One can observe that, for values of b_1 above 1.5 the porosity results very large even at depths of the order of c or less, which appears to be quite unrealistic. While this analysis will consider a range for b_1 values between 1 and 2, it is thus important to bear in mind that values of such parameter above 1.5 do not seem quite realistic.

With respect to the compressibility model (41), any positive value of λ produces a viable distribution of $c_M(z)$ that does not violate any porosity constraints, of course provided that $0 \leq \phi_{min} \leq \phi_0 \leq 1$. Therefore λ can theoretically vary over several orders of magnitude. Still, there appear to be practical limitations for the selection of λ. Figure 10 shows profiles of c_M and ϕ vs. z according to an exponential model (Eqs. (33) and (36)) with porosities ϕ_0=0.45 and ϕ_{min}=0.05, and increasing values of λ. One can observe that values of λ lower than c produce a basin compressibility that varies dramatically along the depth (λ is proportional to the negative slope of the c_M vs. z profile on a semi-log plot), with extremely high values at shallow depth, and unrealistically low values at large depth. While this analysis will consider a range of λ values

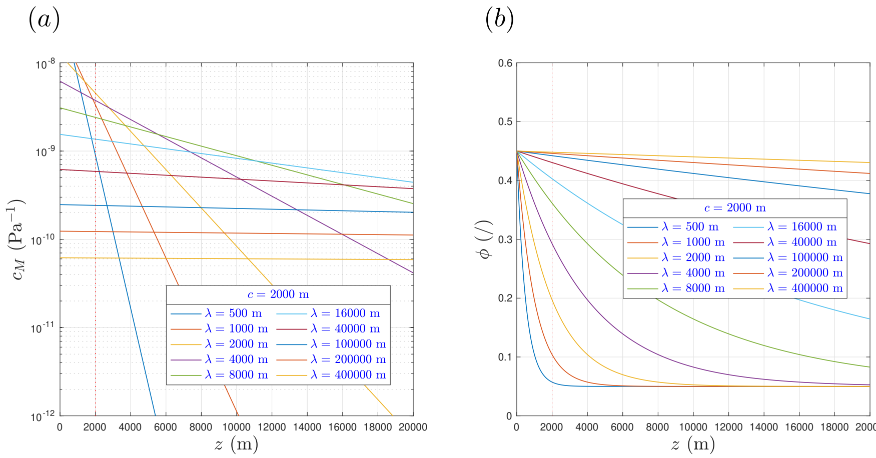

Figure 10: Profiles of (a) c_M vs. z and (b) ϕ vs. z according to an exponential model with increasing values of λ, for a reference NoS depth $c = 2000$ m. In each instance, the porosity is assumed to decrease from a surficial value of 0.45 to 0.05 at large depth.

between $0.25{\cdot}c$ and $200{\cdot}c$, one must be aware that scenarios where $\lambda \leq c$ are seemingly unrealistic.

3.1.5. Fitting Parameter Functions

In order to derive close form expressions of the coefficients α_h, β_h, α_v, and β_v as function of the parameters b_1, for the compressibility model (41), and λ', for the compressibility model (43), the FE model SUBAXS is run under the numerical setup presented in Section 3.1.1 for a series of heterogeneous c_M scenarios identified by a set of b_1 and λ' values. For each of these scenarios, the normalized surface displacement components obtained numerically are fitted by the normalized NoS Eqs. (45) by applying systematically the regression approach presented in Section 3.1.3. The regression results are presented in Tables 1 and 2. In the case of the compressibility model (41), 11 values of b_1 are selected, spanning between 1.001 and 2. In the case of the compressibility model (43), 25 values of λ' are selected, spanning between 0.25 and 200.

The analysis of Tables 1 and 2 reveals that all coefficients tend to vary smoothly and regularly, which suggests it is possible to derive closed-form ex-

Table 1: Fit coefficients α_h, β_h, α_v, and β_v calculated by minimizing Eqs. (47) for power compressibility laws (Eq. 41) characterized by the b_1 values given in the first column.

b_1 (/)	α_h (/)	β_h (/)	α_v (/)	β_v (/)
1.001	2.99734	-2.00225	1.49669	-2.00432
1.010	3.01676	-2.00602	1.49865	-2.00662
1.050	3.10309	-2.02266	1.50686	-2.01636
1.100	3.21097	-2.04310	1.51600	-2.02741
1.150	3.31875	-2.06315	1.52393	-2.03718
1.200	3.42631	-2.08281	1.53066	-2.04568
1.250	3.53361	-2.10208	1.53623	-2.05288
1.500	4.06324	-2.19262	1.54758	-2.06925
1.750	4.57535	-2.27356	1.53386	-2.05236
2.000	5.06298	-2.34510	1.49829	-2.00229

pressions of each of them as a function of the parameters b_1 and λ' using a non-linear regression approach. This is achieved by employing the same trust-region-reflective algorithm (Coleman and Li, 1996) adopted in Section 3.1.3.

Particular care is taken in the selection of the regression models. In the case of the data presented in Table 1, a polynomial equation is adopted. The corresponding expressions for the fitting functions are a follows:

$$\begin{aligned} &\alpha_h\left(b_1\right) = +0.72830 + 2.35740 \cdot b_1 - 0.09090 \cdot b_1^2 \\ &\beta_h\left(b_1\right) = -1.50392 - 0.57540 \cdot b_1 + 0.07749 \cdot b_1^2 \\ &\alpha_v\left(b_1\right) = +0.98655 + 0.83514 \cdot b_1 - 0.36083 \cdot b_1^2 + 0.03561 \cdot b_1^3 \\ &\beta_v\left(b_1\right) = -1.47798 - 0.78966 \cdot b_1 + 0.26372 \cdot b_1^2 \\ &1 < b_1 \leq 2 \end{aligned} \tag{50}$$

The regression results are also visualized in Figure 11. Note that (Eqs. 50) the polynomial degree on b_1 is 2 for the three coefficients α_h, β_h, and β_v, whereas for the coefficient α_v a degree equal to 3 is necessary. For all coefficients, the regression produces a coefficient of determination $R^2 \cong 1$, which indicates a practically perfect fit to the data.

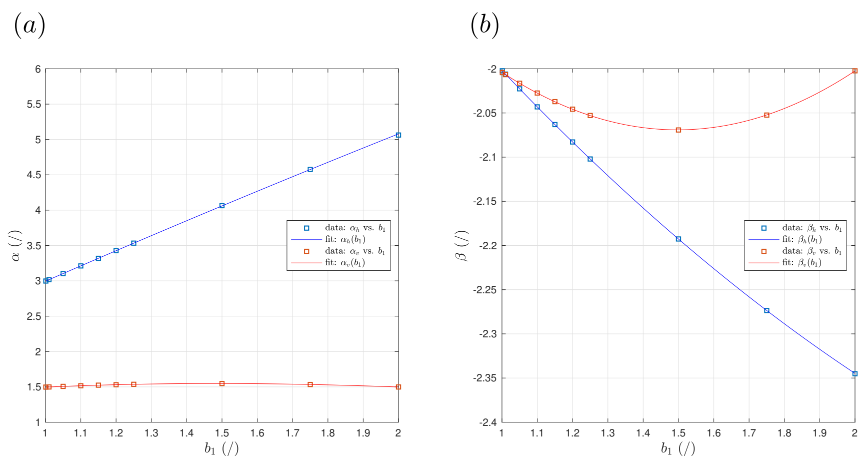

Figure 11: Fitted profiles for the coefficients (a) α_h and α_v, and (b) β_h and β_v, as functions of the power coefficient b_1. The expressions for the fitting functions are given in Eqs. (50).

The data given in Table 2 show a more irregular behaviour than those in Table 1, and thus require devising a more complex regression model. In such case, the chosen fitting type function for each of the coefficients α_h, β_h, α_v and β_v, is the following:

$$f(\lambda') = q + \sum_{i=1}^{4} m_i \cdot \lambda'^{p_i} \tag{51}$$

where q is a fixed constant, m_i and p_i (i=1,..,4) are regression coefficients, with $p_i < 0$. The model (51) consists of a linear combination of four power functions plus a constant. The choice of the model (51) is driven by the observation that, for large values of λ', the compressibility $c_M(z)$ tends to be homogeneous (see Figure 10a) and thus the modified NoS normalized displacement Eqs. (45) must tend asymptotically to Eqs. (39). For this to happen, α_h and α_v should tend to 1, and β_h and β_v should tend to -1.5 for $\lambda' \to \infty$, which is confirmed by the regression results reported in Table 2.

Adopting power functions with negative exponents (*i.e.* $m_i \cdot \lambda'^{p_i}$) allows for ensuring that any linear combination of them will tend asymptotically to zero, so that $f(\lambda') \to q$ for $\lambda' \to \infty$. Therefore, in order to ensure that the regression models may fit the data in Table 2, a constant value $q = 1$ is imposed to fit the coefficients α_h and α_v, and a constant value of $q = -1.5$ is imposed for the coefficients β_h and β_v.

(a) (b)

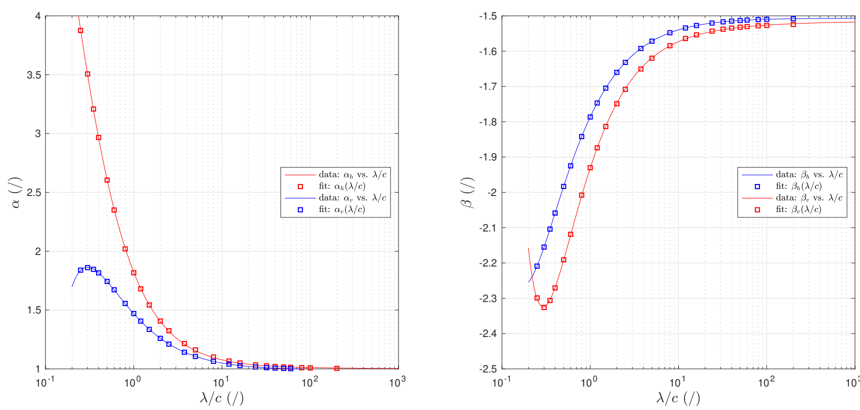

Figure 12: Fitted profiles for the coefficients (a) α_h and α_v, and (b) β_h and β_v, as functions of the coefficient λ scaled to the NoS depth c. The expressions for the fitting functions are given in Eqs. (52).

The regression results are plotted in Figure 12. The corresponding expressions for the fitting functions are the following:

$$
\begin{aligned}
\alpha_h(\lambda') &= +1.0 + 0.09695 \cdot \lambda'^{-0.43427} - 0.14667 \cdot \lambda'^{-0.66569} + \\
&\quad + 1.23850 \cdot \lambda'^{-1.17592} - 0.36648 \cdot \lambda'^{-1.57385} \\
\beta_h(\lambda') &= -1.5 - 0.00702 \cdot \lambda'^{-0.00658} + 0.00663 \cdot \lambda'^{-0.50859} + \\
&\quad - 0.39860 \cdot \lambda'^{-1.01653} + 0.11240 \cdot \lambda'^{-1.51377} \\
\alpha_v(\lambda') &= +1.0 - 0.02142 \cdot \lambda'^{-0.20560} + 0.02882 \cdot \lambda'^{-0.63825} + \\
&\quad + 0.81722 \cdot \lambda'^{-1.08414} - 0.35519 \cdot \lambda'^{-1.50920} \\
\beta_v(\lambda') &= -1.5 - 0.02460 \cdot \lambda'^{-0.06125} - 0.11286 \cdot \lambda'^{-0.63908} + \\
&\quad - 0.49834 \cdot \lambda'^{-1.22379} + 0.20450 \cdot \lambda'^{-1.71945} \\
&\lambda \geq 0.25
\end{aligned}
\tag{52}
$$

Even in this case, the regression produces a coefficient of determination $R^2 \cong 1$ for all coefficients, which indicates a practically perfect fit to the data.

4. Land Subsidence Surrogate Model

The surrogate NoS Eqs. (46) represent Green functions that can be used to calculate the surface displacement field associated with any generic pore pressure change distribution occurring in the subsurface. Based on the assumption of linear elasticity, the principle of linear superposition holds, and the surface displacement components (U_x, U_y, U_z) at any generic location (x, y) and time t are given by the following volume integrals:

$$\begin{aligned}
U_x(x,y,t) &= \int_\Omega \frac{c_M^*(c)\cdot(1-\nu)}{\pi\cdot c^2}\cdot\alpha_h\cdot\frac{r\cdot\eta_x}{c}\cdot\left[1+\left(\frac{r}{c}\right)^2\right]^{\beta_h}\cdot\Delta p_t\cdot d\Omega \\
U_y(x,y,t) &= \int_\Omega \frac{c_M^*(c)\cdot(1-\nu)}{\pi\cdot c^2}\cdot\alpha_h\cdot\frac{r\cdot\eta_y}{c}\cdot\left[1+\left(\frac{r}{c}\right)^2\right]^{\beta_h}\cdot\Delta p_t\cdot d\Omega \qquad (53)\\
U_z(x,y,t) &= \int_\Omega \frac{c_M^*(c)\cdot(1-\nu)}{\pi\cdot c^2}\cdot\alpha_v\cdot\left[1+\left(\frac{r}{c}\right)^2\right]^{\beta_v}\cdot\Delta p_t\cdot d\Omega
\end{aligned}$$

where Ω represents a 3D region of the subsurface where a pore pressure Δp change occurs (*e.g.* an aquifer or a reservoir). Note that $\Delta p_t = \Delta p(x', y', c, t)$ with $(x', y', c) \in \Omega$, and $d\Omega = dx'dy'dc$. In Eqs. (53), r and (η_x, η_y) are the length and the cosine directors of the 2D vector $(x - x', y - y')$.

For a compressibility power model, $c_M^*(c)$ is given by Equation (40), and Eqs. (53) can be rearranged to:

$$\begin{aligned}
U_x(x,y,t) =& e_1\cdot\alpha_h(b_1)\cdot\int_\Omega \frac{r\cdot\eta_x\cdot\left[1+\left(\frac{r}{c}\right)^2\right]^{\beta_h(b_1)}}{c^{b_1+3}}\cdot\Delta p_t\cdot d\Omega \\
U_y(x,y,t) =& e_1\cdot\alpha_h(b_1)\cdot\int_\Omega \frac{r\cdot\eta_y\cdot\left[1+\left(\frac{r}{c}\right)^2\right]^{\beta_h(b_1)}}{c^{b_1+3}}\cdot\Delta p_t\cdot d\Omega \qquad (54)\\
U_z(x,y,t) =& e_1\cdot\alpha_v(b_1)\cdot\int_\Omega \frac{\left[1+\left(\frac{r}{c}\right)^2\right]^{\beta_v(b_1)}}{c^{b_1+2}}\cdot\Delta p_t\cdot d\Omega
\end{aligned}$$

where $e_1 = \frac{(b_1-1)\cdot(1-\nu)}{\pi\cdot a_1\cdot b_1}$, and the coefficients $\alpha_h(b_1)$, $\beta_h(b_1)$, $\alpha_v(b_1)$ and $\beta_v(b_1)$ are given by the Eqs. (50).

For a compressibility exponential model, $c_M^*(c)$ is given by Equation (42), and Eqs. (53) become:

$$\begin{aligned}
U_x\left(x,y,t\right) &= e_2 \cdot \int_\Omega \frac{r \cdot \eta_x \cdot e^{-\frac{c}{\lambda}} \cdot \alpha_h\left(\frac{\lambda}{c}\right)}{c^3} \cdot \left[1+\left(\frac{r}{c}\right)^2\right]^{\beta_h\left(\frac{\lambda}{c}\right)} \cdot \Delta p_t \cdot d\Omega \\
U_y\left(x,y,t\right) &= e_2 \cdot \int_\Omega \frac{r \cdot \eta_y \cdot e^{-\frac{c}{\lambda}} \cdot \alpha_h\left(\frac{\lambda}{c}\right)}{c^3} \cdot \left[1+\left(\frac{r}{c}\right)^2\right]^{\beta_h\left(\frac{\lambda}{c}\right)} \cdot \Delta p_t \cdot d\Omega \\
U_z\left(x,y,t\right) &= e_2 \cdot \int_\Omega \frac{e^{-\frac{c}{\lambda}} \cdot \alpha_v\left(\frac{\lambda}{c}\right)}{c^2} \cdot \left[1+\left(\frac{r}{c}\right)^2\right]^{\beta_v\left(\frac{\lambda}{c}\right)} \cdot \Delta p_t \cdot d\Omega
\end{aligned} \tag{55}$$

where $e_2 = \frac{(\phi_0-\phi_{min})\cdot(1-\nu)}{\pi\cdot(\rho_s-\rho_w)\cdot g\cdot\lambda}$ and the coefficients $\alpha_h\left(\frac{\lambda}{c}\right)$, $\beta_h\left(\frac{\lambda}{c}\right)$, $\alpha_v\left(\frac{\lambda}{c}\right)$ and $\beta_v\left(\frac{\lambda}{c}\right)$ are given by the Eqs. (52).

4.1. Model Implementation and Testing

The implementation of the surrogate land subsidence model relies on the solution of the integrals (54-55), which is carried out numerically by discretizing the domain Ω with an irregular grid whose resolution needs to be generally varied in relation to the spatial gradients of Δp. Note that Ω does not represent the full subsurface system, but only the portion of it where a pore pressure change is observed or simulated.

To validate the model, the case of a horizontal disk-shaped reservoir (Fig. 14) is considered. Such a reservoir has a 2000 m radius, a 20 m thickness, an average depth of 2000 m, and is subject to a uniform pore pressure change of 2 MPa. Three hypothetical sedimentary basin scenarios are considered: a homogeneous system with $c_M^* = 1\times10^{-9}Pa^{-1}$; a heterogeneous system characterized by the compressibility model (41) with $c_{M,1}^* = 1\times10^{-9}Pa^{-1}$ and $b_1 = 1.0291$; and a heterogeneous system characterized by the compressibility model (43) with $c_{M,2}^* = 1\times10^{-9}Pa^{-1}$ and $\lambda = 3850\ m$. The $c_M(z)$ profiles associated with these three scenarios are graphed in Figure 13.

The disk-shaped reservoir is discretized with a mesh consisting of N_e = 4532 prismatic elements with triangular base, which allows for splitting each of the integrals (53) into the sum of as many terms. The surface displacement components are calculated at the N_n nodes of a surface grid, either regular or

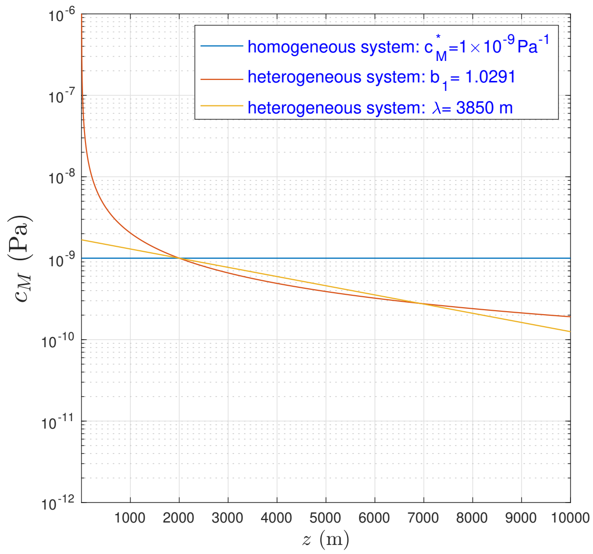

Figure 13: c_M vs. z profiles for a homogeneous basin with $c^*_M = 1 \times 10^{-9} Pa^{-1}$, and two heterogeneous basins with $b_1 = 1.0291$ (Eq. 41), and $\lambda = 3850\ m$ (Eq. 43). The c^*_M value at the depth $c = 2000\ m$ is the same in all scenarios.

irregular, as represented in Figure 14. Note that the reservoir mesh and the surface grid are independent from one another, and it is possible to reduce the surface grid to just a few points of interest where one might want to evaluate the displacement (U_x, U_y, U_z).

Using a matrix notation, the surface displacements can be expressed as:

$$\begin{bmatrix} \mathbf{U}_x \\ \mathbf{U}_y \\ \mathbf{U}_z \end{bmatrix} = \begin{bmatrix} \mathbf{M}_x \\ \mathbf{M}_y \\ \mathbf{M}_z \end{bmatrix} \cdot \mathbf{F} \tag{56}$$

where: $\mathbf{U}_x$, $\mathbf{U}_y$ and $\mathbf{U}_y$ are three $N_n \times 1$ vectors including the displacement components at the surface points; $\mathbf{F}$ is a $N_e \times 1$ vector, whose generic jth component equals the product $V_j \cdot \Delta p_j$, where V_j is the volume of element j (j=1,..,N_e), and Δp_j is average pore pressure change in it; $\mathbf{M}_x$, $\mathbf{M}_y$, and $\mathbf{M}_z$ are $N_n \times N_e$ matrices, whose generic $m_{i,j}$ coefficient are linked to the values of NoS surface

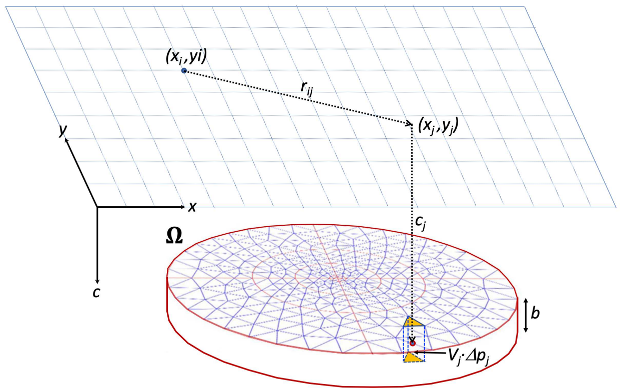

Figure 14: Schematic of the NoS based simulator, representing the reservoir system and the surface domain (see Eqs. (49)).

displacement for the radial distance $r_{i,j}$ between the grid node i (i=1,..,N_n) and the element j's centroid, and the element j's depth c_j (Figure 14).

In the case of a c_M compressibility power model, these coefficients are:

$$\begin{aligned}
m_{x\,i,j} &= e_1 \cdot \alpha_h\left(b_1\right) \cdot \frac{r_{i,j} \cdot \eta_{x\,i,j}}{c_j^{b_1+3}} \cdot \left[1+\left(\frac{r_{i,j}}{c_j}\right)^2\right]^{\beta_h(b_1)} \\
m_{y\,i,j} &= e_1 \cdot \alpha_h\left(b_1\right) \cdot \frac{r_{i,j} \cdot \eta_{y\,i,j}}{c_j^{b_1+3}} \cdot \left[1+\left(\frac{r_{i,j}}{c_j}\right)^2\right]^{\beta_h(b_1)} \\
m_{z\,i,j} &= e_1 \cdot \alpha_v\left(b_1\right) \cdot \frac{1}{c_j^{b_1+2}} \left[1+\left(\frac{r_{i,j}}{c_j}\right)^2\right]^{\beta_h(b_1)}
\end{aligned} \tag{57}$$

whereas in the case of a c_M compressibility exponential model, these coefficients are:

$$\begin{aligned}
m_{x\,i,j} &= e_2 \cdot \alpha_h\left(\frac{\lambda}{c_j}\right) \cdot e^{-\frac{c_j}{\lambda}} \cdot \frac{r_{i,j} \cdot \eta_x}{c_j^3} \cdot \left[1+\left(\frac{r_{i,j}}{c_j}\right)^2\right]^{\beta_h\left(\frac{\lambda}{c_j}\right)} \\
m_{y\,i,j} &= e_2 \cdot \alpha_h\left(\frac{\lambda}{c_j}\right) \cdot e^{-\frac{c_j}{\lambda}} \cdot \frac{r_{i,j} \cdot \eta_y}{c_j^3} \cdot \left[1+\left(\frac{r_{i,j}}{c_j}\right)^2\right]^{\beta_h\left(\frac{\lambda}{c_j}\right)} \\
m_{z\,i,j} &= e_2 \cdot \alpha_v\left(\frac{\lambda}{c_j}\right) \cdot e^{-\frac{c_j}{\lambda}} \cdot \frac{1}{{c_j}^2} \cdot \left[1+\left(\frac{r_{i,j}}{c_j}\right)^2\right]^{\beta_v\left(\frac{\lambda}{c_j}\right)}
\end{aligned} \tag{58}$$

Eq. (56), together with Eqs. (57-58), indicate that the surrogate surrogate land subsidence model relies substantially on a "response-matrix" approach, where the coefficients of the matrix $[\mathbf{U}_y \mathbf{U}_y \mathbf{U}_z]^T$ depend on the characteristics of the mesh discretizing Ω, and the modified NoS Eqs. (45) which in turn account for the basin compressibility model. It is worth noting that, in the numerical calculation of the integrals (54-55), the resolution of the reservoir mesh needs to be high enough to minimize the truncation errors introduced by neglecting the variability of $r_{i,j}$ and c_j within each element j.

The results of the disk-shapep reservoir tests are summarized in Figure 15, which shows the horizontal and vertical surface displacement components along the radial distance from the center of the cylindric reservoir, for three investigated $c_M(z)$ scenarios. In each subpanel, surface displacements obtained with the surrogate semi-analytical model are compared with those from the numerical model SUBAXS. All tests indicate a satisfactory match between the results of the two approaches, suggesting the surrogate semi-analytical model is sufficiently accurate.

In the homogeneous case (Figs. 15a-b), the surrogate model is truly analytically based since the displacements are calculated assuming a heterogeneous basin with an exponential compressibility model with a very large value of λ. Under these conditions, the fitting functions (52) are such that the surrogate NoS Eqs. (45) are the same as the analytical NoS Eqs. (39). In this case, an analytical solution for a horizontal disk-shaped reservoir subject to a uniform pore pressure change was also derived by Geertsma (1973), and that solution is used here to benchmark the surrogate model (Figs. 15a-b).

Results for the heterogeneous basins (Figs. 15c-f) demonstrate that both the horizontal and the vertical surface displacement are larger than those for the homogeneous basin (Figs. 15a-b). This is due to the differences in the distribution of $c_M(z)$ for the three investigated scenario (see Fig. 13). In these instances, the compressibility c_M^* at the reservoir depth c is the same, but the degree of heterogeneity is significantly different, with both systems exhibiting a larger compressibility in the overburden and a lower one in the underburden than in the homogeneous case. Consequently, the land subsidence, which reflects the three-dimensional effect of propagation of the aquifer compaction up to the surface, is larger for a system that has a more compressible overburden, which happens consistently with the compressibility models shown in Figure 13). The latter shows also that the power model exhibits a much larger compressibility in the overburden than the exponential model, which explains the larger surface displacements observed in Figure 15c-d as compared to those in Figure 15e-f.

5. Conclusions

The surrogate land subsidence model presented in this work applies to normally consolidated sedimentary basins, where the compressibility c_M decreases along the depth according to either power or exponential laws. In Section 2, compressibility models of such types have been investigated and simple equations to derive $c_M(z)$ laws based on overburden gradient data have been derived. It is worth pointing that these equations rely on the assumption of "soft soil", that is a porous medium with a compressibility significantly larger (at least 10 times) than the particle compressibility c_s.

The surrogate land subsidence model applies to conditions of linear elasticity and stems from a semi-analytical form of the classic NoS equations extended to heterogeneous systems. Such a model is truly a hybrid between a numerical model and an analytical one, as it uses closed-form parametric expressions for the NoS equations, with parameters that are retrieved numerically using a systematic combination of numerical test results and non-linear regressions as functions of the basin compressibility model parameters.

While the examples presented here consider specifically power or exponential $c_M(z)$ models, it appears quite possible to apply the same approach to develop semi-analytical NoS equations for different compressibility model types, or even for under-consolidated basins during loading-unloading cycles.

One of the strengths of this model lies in its computational parsimony. Built upon the NoS equations and the principle of linear superposition, the model is formulated as an explicit ”response-matrix” scheme, where the forcing terms depend on the spatial distribution of the change in pore pressure in the subsurface, and the matrix coefficients depend on the selected basin compressibility model. The model results quite easy to implement, and can be used estimate the land surface displacement associated with any simulated or observed 3D pore pressure change field. As such, the surrogate model is particularly suited for screening calculations, uncertainty quantification and risk analysis for subsurface development in sedimentary basins.

It is important to recognize that for more general real-world conditions, for example basins in which c_M varies not only vertically but also horizontally, or with more complex (non-linear, elasto-plastic, etc.) constitutive laws, fully numerical models remain the best choice, although their application may be hindered by the limited availability of data needed for their calibration and validation.

6. Acknowledgements

The author is very grateful to Massimiliano Ferronato, from the University of Padova, Italy, for the valuable discussions during the development of this paper. The author also wish to thank two anonymous reviewers for their valuable comments and suggestions.

References

Abidin, H.Z., Andreas, H., Gumilar, I., Wibowo, I.R.R., 2015. On correlation between urban development, land subsidence and flooding phenomena in Jakarta, in: IAHS-AISH Proceedings and Reports, Copernicus GmbH.. pp. 15–20.

Allis, R., Bromley, C., Currie, S., 2009. Update on subsidence at the Wairakei-Tauhara geothermal system, New Zealand. Geothermics 38, 169–180.

Baú, D., Ferronato, M., Gambolati, G., Teatini, P., 2002. Basin-scale compressibility of the Northern Adriatic by the radioactive marker technique. Géotechnique 52, 605–616.

Bear, J., Corapcioglu, M.Y., 1981a. Mathematical model for regional land subsidence due to pumping. 1. Integrated aquifer subsidence equations based on vertical displacement only. Water Resour. Res. 17, 937–946.

Bear, J., Corapcioglu, M.Y., 1981b. Mathematical model for regional land subsidence due to pumping. 2. Integrated aquifer subsidence equations for vertical and horizontal displacement. Water Resour. Res. 17, 947–958.

Biot, M.A., 1941. General theory of three-dimensional consolidation. J. Appl. Phys. 12, 155–164.

Biot, M.A., 1955. Theory of elasticity and consolidation for a porous anisotropic solid. J. Appl. Phys. 26, 182–185.

Biot, M.A., Willis, D.G., 1957. The elastic coefficients of the theory of consolidation. J. Appl. Mech. 24, 594–601.

Castellazzi, P., Arroyo-Domínguez, N., Martela, R., Calderhead, A.I., Normand, J.C.L., Gárfias, J., Rivera, A., 2016. Land subsidence in major cities of Central Mexico: Interpreting InSAR-derived land subsidence mapping with hydrogeological data. Int. J. Appl. Earth Obs. 47, 102–111. doi:https://doi.org/10.1016/j.jag.2015.12.002.

Cian, F., Blasco, J.M.D., Carrera, L., 2019. Sentinel-1 for Monitoring Land Subsidence of Coastal Cities in Africa Using PSInSAR: A Methodology Based on the Integration of SNAP and StaMPS. Geosci. 9, 124. doi:https://doi.org/10.3390/geosciences9030124.

Coleman, T., Li, Y., 1996. An interior, trust region approach for nonlinear minimization subject to bounds. SIAM J. Optim. 6, 418–445.

Ellis, D.V., Singer, J.M., 2008. Well Logging for Earth Scientists (2nd Ed.). Springer, Dordrecht.

Erban, L., Gorelick, S.M., Zebker, H.A., 2014. Groundwater extraction, land subsidence, and sea-level rise in the Mekong Delta, Vietnam. Environ. Res. Let. 9, 084010, doi:10.1088/1748–9326/9/8/084010.

Ferronato, M., Gambolati, G., Teatini, P., Baù, D., 2003. Interpretation of radioactive marker measurements to evaluate compaction in the Northern Adriatic gas fields. SPE Reserv. Eval. Eng. 6, 401–411.

Fokker, P.A., van Leijen, F.J., Orlic, B., van der Marel, H., Hanssen, R.F., 2018. Subsidence in the Dutch Wadden Sea. Netherlands Journal of Geosciences 97, 129–181. doi:10.1017/njg.2018.9.

Galloway, D.L., Burbey, T.J., 2011. Review: Regional land subsidence accompanying groundwater extraction. Hydrogeol. J. 19, 1459—1486.

Gambolati, G., Ferronato, M., Teatini, P., Deidda, R., Lecca, G., 2001. Finite element analysis of land subsidence above depleted reservoirs with pore pressure gradient and total stress formulations. Int. J. Numer. Anal. Meth. Geomech. 25, 307–327.

Gambolati, G., Ricceri, G., Bertoni, W., Brighenti, G., Vuillermin, E., 1991. Mathematical simulation of the subsidence of Ravenna. Water Resour. Res. 27, 2899–2918.

Gambolati, G., Teatini, P., 2015. Geomechanics of subsurface water withdrawal and injection. Water Resour. Res. 51, 3922–3955. doi:doi:10.1002/2014WR016841.

Geertsma, J., 1966. Problems of rock mechanics in petroleum production engineering, in: Proceedings of 1st Cong. Int. Soc. Rock Mechan.. International Society for Rock Mechanics and Rock Engineering, Lisbon, pp. 585–594.

Geertsma, J., 1973. A basic theory of subsidence due to reservoir compaction: The homogenous case. Verhandelingen Kon. Ned. Geol. Mijnbouwk. Gen. 28, 43–62.

González, P.J., Tiampo, K.F., Palano, M., Cannavó, F., Fernández, J., 2012. The 2011 lorca earthquake slip distribution controlled by groundwater crustal unloading. Nat. Geosci. 5, 821–825.

Ikuemonisan, F.E., Ozebo, V.C., 2020. Characterisation and mapping of land subsidence based on geodetic observations in Lagos, Nigeria. Geod. Geodyn. 11, 151–162.

Jayeoba, A., Mathias, S.A., Nielsen, S., Vilarrasa, V., Bjørnarå, T.I., 2019. Closed-form equation for subsidence due to fluid production from a cylindrical confined aquifer. J. Hydrol. 573, 964–969.

Jha, B., Bottazzi, F., Wojcik, R., Coccia, M., Bechor, N., McLaughlin, D., Herring, T., Hager, B.H., Mantica, S., Juanes, R., 2015. Reservoir characterization in an underground gas storage field using joint inversion of flow and geodetic data. International Journal for Numerical and Analytical Methods in Geomechanics 39, 1619–1638. URL: https://onlinelibrary.wiley.com/doi/abs/10.1002/nag.2427, doi:https://doi.org/10.1002/nag.2427, arXiv:https://onlinelibrary.wiley.com/doi/pdf/10.1002/nag.2427.

Kasmarek, M.C., Ramage, J.K., Johnson, M.R., 2016. Water-level altitudes 2016 and water-level changes in the Chicot, Evangeline, and Jasper aquifers and compaction 1973–2015 in the Chicot and Evangeline aquifers, Houston-Galveston region, Texas. U.S. Geological Survey Scientific Investigations Map 3365 pamphlet, 16 sheets, scale 1:100,000. http://dx.doi.org/10.3133/sim3365.

Kulp, S.A., Strauss, B.H., 2019. New elevation data triple estimates of global vulnerability to sea-level rise and coastal flooding. Nature Communications 10, 4844. URL: https://doi.org/10.1038/s41467-019-12808-z, doi:10.1038/s41467-019-12808-z.

de Luna, R.M.R., Garnés, S.J.A., Cabral, J.J.S.P., Pereira, J.J.S., dos Santos, S.M., 2017. Groundwater overexploitation and soil subsidence monitoring on Recife plain (Brazil). Natural Hazards 86, 1363–1376. URL: https://doi.org/10.1007/s11069-017-2749-y, doi:10.1007/s11069-017-2749-y.

Mindlin, R., 1936. Force at a point in the interior of a semi-infinite solid. Phys. 7, 195–202.

Mindlin, R., Chen, D., 1950. Nuclei of strain in the semi-infinite solid. J. Appl. Phys. 21, 926. doi:https://doi.org/10.1063/1.1699785.

Morita, N., Whitfill, D.L., Nygaard, ., Bale, A., 1989. A quick method to determine subsidence, reservoir compaction, and in-situ stress induced by reservoir depletion. J. Petrol. Technol. 41, 71–79.

Ng, A.H., Ge, L., Li, X., 2015. Assessments of land subsidence in the Gippsland Basin of Australia using ALOS PALSAR data. Remote Sens. Environ. 159, 86–101.

Ortiz-Zamora, D., Ortega-Guerrero, A., 2010. Evolution of long-term land subsidence near Mexico City: Review, field investigations, and predictive simulations. Water Resour. Res. 46. doi:doi:10.1029/2008WR007398.

Sharma, B.D., 1956. Stresses in an infinite slab due to a nucleus of thermoelastic strain in it. Z. Angew. Math. Mech. 36, 565–589.

Sneed, M., Brandt, J.T., Solt, M., 2018. Land subsidence along the California Aqueduct in west-central San Joaquin Valley, California, 2003–10. U.S. Geological Survey Scientific Investigations Report 2018–5144. https://doi.org/10.3133/sir20185144.

Teatini, P., Castelletto, N., Ferronato, M., Gambolati, G., Janna, C., Cairo, E., Marzorati, D., Colombo, D., Ferretti, A., Bagliani, A., Bottazzi, F., 2011. Geomechanical response to seasonal gas storage in depleted reservoirs: A case study in the po river basin, italy. Journal of Geophysical Research: Earth

Surface 116. URL: https://agupubs.onlinelibrary.wiley.com/doi/abs/10.1029/2010JF001793, doi:https://doi.org/10.1029/2010JF001793, arXiv:https://agupubs.onlinelibrary.wiley.com/doi/pdf/10.1029/2010JF001793.

Teatini, P., Ferronato, M., Gambolati, G., Gonella, M., 2006. Groundwater pumping and land subsidence in the emilia-romagna coastland, italy: Modeling the past occurrence and the future trend. Water Resour. Res. 42. doi:doi:10.1029/2005WR004242.

Teatini, P., Tosi, L., Strozzi, P., 2012. Comment on "Recent subsidence of the Venice Lagoon from continuous GPS and interferometric synthetic aperture radar" by Y. Bock, S. Wdowinski, A. Ferretti, F. Novali, and A. Fumagalli. Geochem. Geophys. Geosyst. 13. doi:Q07008,doi:10.1029/2012GC004191.

Tempone, P., Fjær, E., Landrø, M., 2010. Improved solution of displacements due to a compacting reservoir over a rigid basement. Appl. Math. Model. 34, 3352–3362.

Terzaghi, K., 1936. The shearing resistance of saturated soils and the angle between the planes of shear. First Int. Conf. Soil Mech., Harvard University, 1, 54–56.

van Opstal, G.H.C., 1974. The effect of base-rock rigidity on subsidence due to reservoir compation, in: IIIrd Conf. on Rock Mechanics, Denver (CO). pp. 1102–1111.

Verruijt, A., 1969. Elastic storage of aquifers, in: De Wiest, R. (Ed.), Flow Through Porous Media, Academic Press, New York. pp. 331–376.

Wang, Y.Q., Wang, Z.F., Cheng, W.C., 2019. A review on land subsidence caused by groundwater withdrawal in Xian, China. B. Eng. Geol. Environ. 78, 2581–2863.

Zisman, W.A., 1933. Young's modulus and Poisson's Ratio with Reference to Geophysical Applications. PNAS 19, 653–665.

Table 2: Fit coefficients α_h, β_h, α_v, and β_v calculated by minimizing Eqs. (47) for exponential compressibility laws (Eq. 43) characterized by the λ' values given in the first column.

λ' (/)	α_h (/)	β_h (/)	α_v (/)	β_v (/)
0.25	3.87569	-2.20892	1.83910	-2.29899
0.30	3.50634	-2.15502	1.86068	-2.32587
0.35	3.20810	-2.10415	1.84590	-2.30632
0.40	2.96651	-2.05858	1.81586	-2.27062
0.50	2.60465	-1.98320	1.74301	-2.19087
0.60	2.34999	-1.92486	1.67230	-2.11877
0.80	2.01967	-1.84198	1.55617	-2.00776
1.00	1.81680	-1.78647	1.47040	-1.93010
1.20	1.68035	-1.74680	1.40604	-1.87369
1.50	1.54339	-1.70477	1.33571	-1.81343
2.00	1.40640	-1.66011	1.25921	-1.74900
2.50	1.32438	-1.63189	1.21032	-1.70810
3.75	1.21548	-1.59237	1.14161	-1.65048
5.00	1.16131	-1.57175	1.10575	-1.62013
8.00	1.10067	-1.54783	1.06422	-1.58460
12.00	1.06714	-1.53422	1.04059	-1.56417
16.00	1.05043	-1.52734	1.02862	-1.55375
24.00	1.03375	-1.52040	1.01656	-1.54321
32.00	1.02543	-1.51691	1.01049	-1.53789
40.00	1.02044	-1.51482	1.00683	-1.53468
50.00	1.01645	-1.51313	1.00390	-1.53211
60.00	1.01379	-1.51201	1.00194	-1.53039
80.00	1.01047	-1.51061	0.99949	-1.52823
100.00	1.00848	-1.50976	0.99802	-1.52693
200.00	1.00450	-1.50807	0.99507	-1.52433

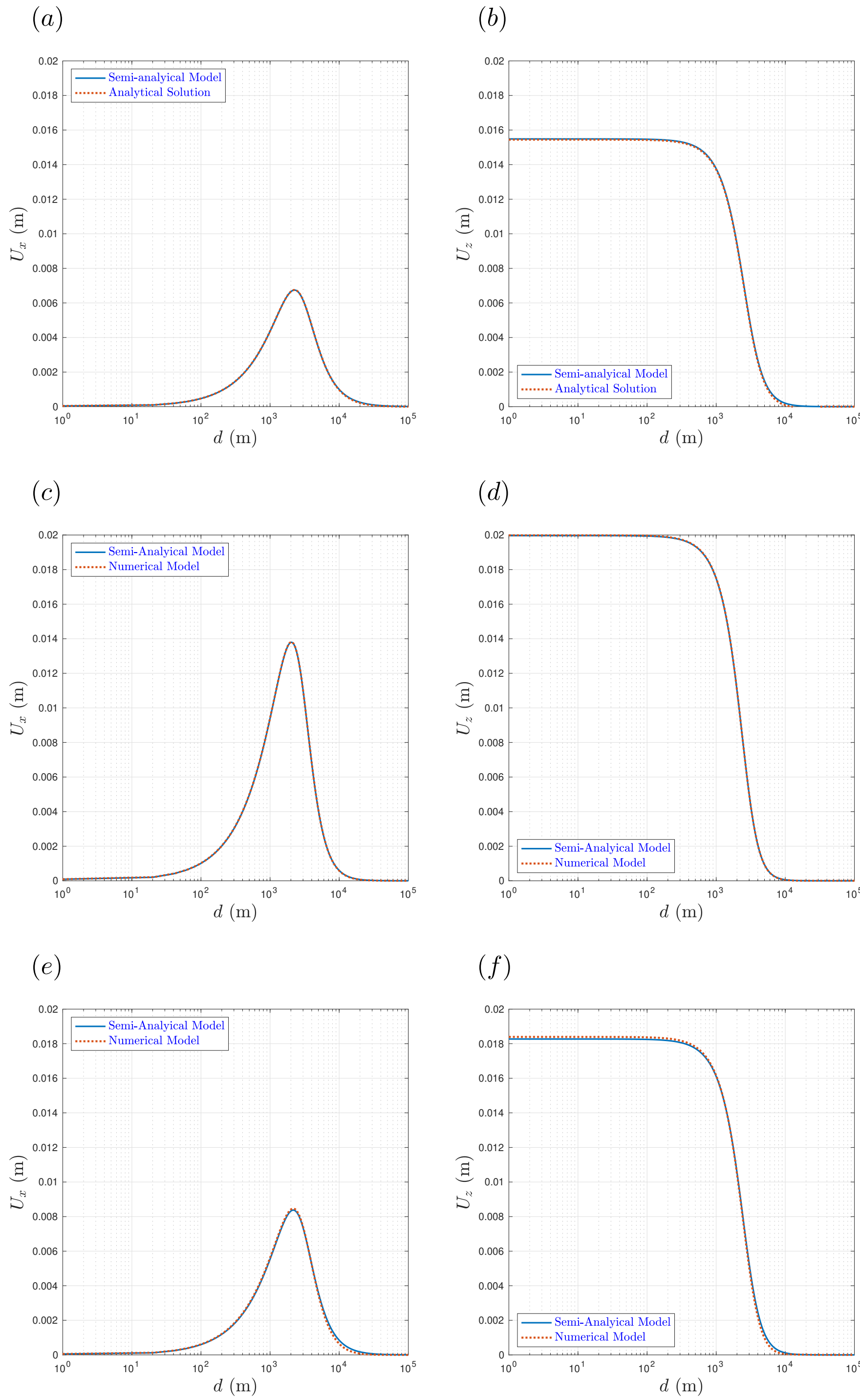

Figure 15: Profiles of the surface displacement components u_r and u_z vs. the radial distance r, obtained using the surrogate semi-analytical model and the numerical model SUBAXS assuming (subpanels (a-b)) an homogeneous system, and and a heterogeneous system with (subpanels (c-d)) $b_1 = 1.0291$ and (subpanels (e-f)) $\lambda = 3850\, m$. Note that in the homogeneous case (subpanels (a-b)) the surrogate model is truly based on the classic NoS equations (39), and its solution is compared to the analytical model derived by Geertsma (1973).